

Magnetic-buoyancy-induced mixing in AGB Stars: fluorine nucleosynthesis at different metallicities

D. Vescovi^{1,2,3}, S. Cristallo^{3,2}, S. Palmerini^{4,2}, C. Abia⁵, and M. Busso^{4,2}

¹ Goethe University Frankfurt, Max-von-Laue-Strasse 1, Frankfurt am Main 60438, Germany
e-mail: vescovi@iap.uni-frankfurt.de

² INFN, Section of Perugia, Via A. Pascoli snc, 06123 Perugia, Italy

³ INAF, Observatory of Abruzzo, Via Mentore Maggini snc, 64100 Teramo, Italy

⁴ Department of Physics and Geology, University of Perugia, via A. Pascoli snc, 06123 Perugia, Italy

⁵ University of Granada, Departamento de Fisica Teorica y del Cosmos, 18071 Granada, Spain

Received ; accepted

ABSTRACT

Asymptotic giant branch (AGB) stars are considered to be among the most significant contributors to the fluorine budget in our Galaxy. While at close-to-solar metallicity observations and theory agree, at lower metallicities stellar models overestimate the fluorine production with respect to heavy elements. We present ^{19}F nucleosynthesis results for a set of AGB models with different masses and metallicities in which magnetic buoyancy acts as the driving process for the formation of the ^{13}C neutron source (the so-called ^{13}C pocket). We find that ^{19}F is mainly produced as a result of nucleosynthesis involving secondary ^{14}N during convective thermal pulses, with a negligible contribution from the ^{14}N present in the ^{13}C pocket region. A large ^{19}F production is thus prevented, resulting in lower fluorine surface abundances. As a consequence, AGB stellar models with magnetic-buoyancy-induced mixing at the base of the convective envelope well agree with available fluorine spectroscopic measurements at both low and close-to-solar metallicity.

Key words. Stars: abundances – Stars: AGB and post-AGB – Stars: magnetic field – Magnetohydrodynamics (MHD) – Stars: carbon – Nuclear reactions, nucleosynthesis, abundances

1. Introduction

Understanding the cosmic origin of fluorine is one of the most interesting topics in the nuclear astrophysics field. The production of its sole stable isotope, ^{19}F , largely depends from the physical conditions characterizing stellar interiors. To date, it is widely debated which is the primary source of fluorine in the Universe and several sites have been proposed as potential candidates: AGB stars (Forestini et al. 1992), rapidly rotating massive stars (Limongi & Chieffi 2018), Wolf-Rayet stars (Meynet & Arnould 2000), core-collapse supernovae (Woosley & Haxton 1988), and novae (José & Hernanz 1998). While the contributions from many of these sources are required to explain the galactic chemical evolution of fluorine abundance (see e.g. Meynet & Arnould 2000; Renda et al. 2004; Kobayashi et al. 2011; Spitoni et al. 2018; Prantzos et al. 2018; Olive & Vangioni 2019; Grisoni et al. 2020), the only direct observation of fluorine production is provided by spectroscopic findings of photospheric $[\text{F}/\text{Fe}]$ enhancements in intrinsic AGB carbon stars (Jorissen et al. 1992; Abia et al. 2009, 2010, 2011, 2019) and metal-poor extrinsic stars (Lutcatello et al. 2011; Abia et al. 2019).

AGB stars consist of a degenerate C-O core, surrounded by a He-shell and a H-shell, separated by a He-rich intermediate zone (He-intershell), and an extended convective envelope. Recurrently, on a timescale of tens of thousand years of quiescent H-shell burning, the He-burning shell becomes thermally unstable. The large amount of energy released during this thermal pulse (TP), mainly due to the triple- α reaction, induces convective motions throughout the He-intershell and causes an expansion, and thus a cooling of the H-burning shell. As a con-

sequence, the latter is switched off until the star contracts, and the rising temperature is large enough to its re-ignition. This process repeats up to the complete erosion of the envelope by stellar winds and characterizes the thermally pulsing AGB (TP-AGB) phase of these stars (e.g., Iben & Renzini 1983). During the expansion of the envelope, convection may penetrate deep into the H-He discontinuity beyond the H-burning shell and carry to the surface fresh products of the nucleosynthesis. This phenomenon is known as third dredge-up (TDU). At each TDU episode, protons are partially mixed from the envelope into the He-intershell and, as the H-burning shell reignites, are captured by the abundant ^{12}C nuclei to produce a ^{13}C -enriched layer, the so-called ^{13}C pocket. ^{13}C nuclei are then efficiently burned via the $^{13}\text{C}(\alpha, n)^{16}\text{O}$ reaction at $T \approx 9 \times 10^7$ K (see Cristallo et al. 2018 and references therein), so producing the free neutrons necessary for the synthesis of heavy elements in low mass AGB stars ($M \lesssim 3M_{\odot}$) through the so-called s(low)-process (see Busso et al. 1999; Herwig 2005; Straniero et al. 2006; Karakas & Lattanzio 2014 for reviews). A second neutron burst is driven by the $^{22}\text{Ne}(\alpha, n)^{25}\text{Mg}$, which is efficiently activated at the base of the convective zone produced by a TP when the temperature reaches about 3×10^8 K (mostly in more massive AGBs, see e.g. Karakas & Lattanzio 2014).

During the interpulse phase, part of the neutrons released within the He-intershell are captured by ^{14}N through the $^{14}\text{N}(n, p)^{14}\text{C}$ reaction to synthesize ^{15}N by means of the chain $^{14}\text{C}(\alpha, \gamma)^{18}\text{O}(p, \alpha)^{15}\text{N}$. ^{15}N is then burnt to primary ^{19}F via $^{15}\text{N}(\alpha, \gamma)^{19}\text{F}$ reaction in the subsequent convective TP (Goriely & Mowlavi 2000; Lugaro et al. 2004; Cristallo et al. 2014). An additional contribution to fluorine production comes

from secondary ^{13}C and ^{14}N synthesized in the H-burning ashes and from the eventual unburnt ^{13}C in the pocket (Cristallo et al. 2009b). In both cases, ^{13}C is engulfed in the convective shell generated by the TP and produce further secondary ^{19}F through the same above mentioned reactions chain. Fluorine is then carried to the surface by convective motions during the TDU. Therefore, its envelope abundance is expected to be correlated with those of carbon and *s*-process elements (see Abia et al. 2019 and references therein).

Actually, one of the most debated topics in AGB modeling concerns the formation of the ^{13}C pocket. The solution to this problem is strictly connected to a deep understanding of the physical processes governing mass-exchange at the interface between the convective envelope and the radiative core. Latest research has focused on studying non-convective transport mechanisms, usually ignored by the canonical theory of stellar structure and evolution. Different kinds of additional transport processes were invoked for the penetration of proton-rich material from the convective envelope into the He-intershell: convective overshoot (Herwig et al. 1997), opacity-induced overshoot (Cristallo et al. 2009b, 2011, 2015b), mixing induced by rotation (Herwig et al. 2003; Siess et al. 2004; Piersanti et al. 2013) or internal gravity waves (Denissenkov & Tout 2003; Battino et al. 2016), and magnetic-buoyancy-induced mixing (Trippella et al. 2014, 2016). Focusing on the production of fluorine, it was suggested that a mechanism leading to the formation of an extended ^{13}C pocket and, at the same time, to a small amount of ^{14}N , could solve the problem of ^{19}F overproduction with respect to *s*-elements in low-mass metal-poor objects (Abia et al. 2019).

Post-process neutron-capture models for AGB stars, in which the formation of the required ^{13}C reservoir is ascribed to magnetic-buoyancy-induced mixing, were shown to be able to account for the solar distributions of *s*-only isotopes (Trippella et al. 2016), isotopic ratios of *s*-elements measured in presolar SiC grains (Palmerini et al. 2018) and a large part of abundance observations in evolved low-mass stars (Busso et al. 2021). All the aforementioned works applied the theory of magnetic-induced buoyancy mixing theorized by Nucci & Busso (2014). This theory has recently been adopted by Vescovi et al. (2020), who contextualized magnetic mixing in the more complex framework of FRUITY stellar evolutionary models, obtaining a satisfactory fit to presolar grain isotopic ratios. The same stellar models also provide a consistent explanation for the observed yttrium abundance trends in the Galactic disk's inner region (Magrini et al. 2021). FRUITY Magnetic models predict that deep profiles of low proton abundances are generated below the convective envelope border. The low proton concentration severely limits local ^{14}N formation, as protons are almost entirely consumed for the synthesis of ^{13}C , potentially affecting ^{19}F production as well.

Here we investigate fluorine nucleosynthesis in low-mass AGB stars by computing a new series of stellar models accounting for the formation of a magnetic-buoyancy-induced ^{13}C pocket. The structure of the paper is as follows. In Section 2 we present the stellar evolutionary code, the nuclear network, and the mixing algorithm adopted to calculate the AGB models. In Section 3 we compare our models with available F spectroscopic abundances in a sample of Galactic and extra-Galactic AGB carbon stars, as well as with other metal-poor Ba-type and CH-type evolved stars. Finally, in the last section we summarize our conclusions.

Table 1. Reaction rates of relevance to fluorine nucleosynthesis used in our computations.

Reaction	Reference
$^{14}\text{N}(p, \gamma)^{15}\text{O}$	1
$^{15}\text{N}(p, \gamma)^{16}\text{O}$	2
$^{17}\text{O}(p, \gamma)^{18}\text{F}$	3
$^{18}\text{O}(p, \gamma)^{19}\text{O}$	4
$^{15}\text{N}(p, \alpha)^{12}\text{C}$	5
$^{17}\text{O}(p, \alpha)^{14}\text{N}$	6
$^{18}\text{O}(p, \alpha)^{15}\text{N}$	7
$^{19}\text{F}(p, \alpha)^{15}\text{O}$	8
$^{14}\text{C}(\alpha, \gamma)^{18}\text{O}$	9
$^{14}\text{N}(\alpha, \gamma)^{18}\text{F}$	10
$^{15}\text{N}(\alpha, \gamma)^{19}\text{F}$	10
$^{18}\text{O}(\alpha, \gamma)^{22}\text{Ne}$	10
$^{19}\text{F}(\alpha, p)^{22}\text{Ne}$	11
$^{13}\text{C}(\alpha, n)^{16}\text{O}$	12
$^{14}\text{N}(n, p)^{14}\text{C}$	13

References. (1) Imbriani et al. (2005); (2) Leblanc et al. (2010); (3) Di Leva et al. (2014); (4) Best et al. (2019); (5) Angulo et al. (1999); (6) Bruno et al. (2016); (7) Bruno et al. (2019); (8) Indelicato et al. (2017); (9) Johnson et al. (2009); (10) Iliadis et al. (2010); (11) D'Agata et al. (2018); (12) Trippella & La Cognata (2017); Wallner et al. (2016).

2. Stellar models

The stellar models presented in this work have been computed using the FUNS code (see Straniero et al. 2006 and references therein) by following the chemical evolution of approximately 500 isotopes (from hydrogen to bismuth) linked by more than 800 reactions (charged particle reactions, neutron captures, and β -decays). The baseline nuclear network is essentially the same already described in Cristallo et al. (2009b) with the addition of some recently updated reaction rates. In particular, the list of adopted reaction rates relevant to the nucleosynthesis of fluorine is reported in Table 1.

For radiative opacities, we computed opacity tables by means of the OPAL Web tool¹. At low temperatures ($\log T \leq 4.05$), typical of the external layers of stars, we used the $\text{\AE}SOPUS$ tool (Marigo & Aringer 2009), which includes molecular and atomic species relevant for AGB atmospheres, to compute the opacity tables. In particular, $\text{\AE}SOPUS$ allows to take into account changes in opacity due to both eventual oxygen and α -enhancement (see Table 2) and to chemical composition variations of the envelope when the star becomes carbon-rich (Marigo 2002; Cristallo et al. 2007; Ventura & Marigo 2010). Opacity tables used in this work have been calculated with the scaled-solar element distribution by Lodders (2020). Accordingly, a solar-calibrated value of the mixing length parameter $\alpha_{\text{ml}} = 1.86$ is adopted (see Vescovi et al. 2019 for more details). Regarding the mass-loss rate, we adopted a Reimers' formula with $\eta = 0.4$ for the pre-AGB evolution, and the rate used by Abia et al. (2020) for the AGB phase (such a rate is slightly different with respect to Straniero et al. 2006, due to the adoption of recalculated bolometric corrections).

The surface enrichment of C and *s*-process elements in AGB stars is related to the complex coupling between convective mixing and nuclear processes. The problem of the neutron source in AGB stars, and in particular the physical process driving the formation of a ^{13}C pocket in the He-rich intershell is still a matter of

¹ <https://opalopacity.llnl.gov/new.html>

Table 2. Initial mass, [Fe/H], total metallicity (comprehensive of $\alpha_{\text{O-Ca}}$ enhancements), and helium adopted for the models presented in this work

Mass (M_{\odot})	[Fe/H]	Z	Y	α_{O}	$\alpha_{\text{Ne-Ca}}$
1.5	-2.18	3.10×10^{-4}	0.247	0.7	0.4
1.5	-1.88	5.33×10^{-4}	0.248	0.6	0.4
1.5	-1.70	8.00×10^{-4}	0.248	0.6	0.4
1.5	-1.18	2.13×10^{-3}	0.250	0.5	0.4
2.0	-0.70	5.70×10^{-3}	0.254	0.4	0.3
2.0	-0.40	8.13×10^{-3}	0.257	0.2	0.15
2.0	-0.18	1.00×10^{-2}	0.259	0	0
2.0	+0.05	1.67×10^{-2}	0.267	0	0
2.0	+0.13	2.00×10^{-2}	0.271	0	0

debate (see Section 1). In past FRUITY models, the partial mixing of hydrogen from the envelope necessary to produce fresh ^{13}C was accounted for by the so-called opacity-induced overshoot (Straniero et al. 2006; Cristallo et al. 2009b). This powers an extra-mixing and a formation of a chemically smooth transition zone between the fully convective envelope and the radiative region. At the inner border of the convective envelope, the velocity of the descending material accelerated by convection is estimated as

$$v = v_{\text{cb}} \exp\left(-\frac{\delta r}{\beta H_p}\right), \quad (1)$$

where v_{cb} is the velocity at the convective border, δr is the distance from the border, H_p is the pressure scale height at the convective border, and β is a free parameter whose value was set to 0.1 in order to maximize the s -process production in low-mass AGB stars (see Cristallo et al. 2009b; Guandalini & Cristallo 2013). The free parameter β regulates the amount of protons mixed beyond the bare convective border, and also affects the TDU efficiency. In standard FRUITY models, the partial mixed zone is extended below the formal Schwarzschild convective boundary down to $2 H_p$ (Straniero et al. 2006). Instead, in FRUITY Tail models (Cristallo et al. 2015a) the penetration limit is fixed to the layer where the convective velocity is 10^{-11} times lower than the value attained at the Schwarzschild border. The ensuing ^{13}C pockets were shown to be remarkably larger than those obtained in standard FRUITY models, thus resulting in a substantial increase of surface s -process enrichment.

Vescovi et al. (2020) found that, due the inclusion of updated physical inputs, the slope of the exponential decline of convective velocities has to be reduced down to $\beta = 0.025$ not to alter the efficiency of the TDU and obtain a sizable amount of dredged-up material. However, models computed with such parameter choice show an extra-mixing so inefficient to almost inhibit the production of s -process nuclei. Thus, mixing triggered by magnetic fields has been introduced as an additional mixing mechanism. As in Nucci & Busso (2014), these authors assumed that a toroidal field is present in the radiative He-intershell at the beginning of the TDU and triggers the buoyant rise of magnetic flux tubes. As a consequence, a matter flow is pushed to the envelope. This induces, for mass conservation, a matter down-flow of H-rich material to He-intershell necessary for the formation of the ^{13}C pocket. The down-flow velocity can be expressed as

$$v(r) = u_p \left(\frac{r_p}{r}\right)^{k+2}, \quad (2)$$

where r_p is the distance from the stellar center from which magnetic flux tubes, generated in the He-intershell, start to rise. r_p

can be identified from the critical toroidal B_{φ} necessary for the onset of magnetic buoyancy instabilities (Vescovi et al. 2020). k is the exponent quantifying the density decline, being $\rho(r) \propto r^k$, in the He-rich radiative layers below the convective envelope during a TDU and it is typically lower than -3 (see also Busso et al. 2021). The identification of the critical field necessary for the occurrence of instabilities by magnetic buoyancy allows to identify the corresponding radial position r_p from which magnetic structures arise. u_p is the *effective* starting buoyant velocity. Actually, the magnetized domains are rather fast and occupy only a small fraction of the total mass of the stellar layer ($\approx 1/10^5$, see e.g. Busso et al. 2007; Trippella et al. 2016), thus transporting mass at a rate equal to assuming an *effective* buoyant velocity for all the material in the layer. In Vescovi et al. (2020), it was found that most of the heavy-element isotope ratios measured in presolar SiC grains from AGB stars are consistently explained by stellar AGB models computed with a unique choice for the toroidal field strength and the initial buoyant velocity, namely $B_{\varphi} = 5 \times 10^4$ G and $u_p = 5 \times 10^{-5}$ cm s $^{-1}$. Nonetheless, we expect a non-trivial mass-metallicity dependence of the mixing triggered by magnetic buoyancy (as for other type of mixing, see e.g. Joyce & Chaboyer 2018; Battino et al. 2021). In particular, the toroidal field strength is determined by the differential rotation profile established in the He-intershell and which amplifies the magnetic field via dynamo action (see Section 4). In this framework, the compactness of a star at the pre-AGB and AGB stages is a fundamental property that influences the dynamo process and the following magnetic-buoyancy-induced mixing. The stellar models presented here have H-exhausted core masses at the beginning of the TP-AGB phase very similar to the $2 M_{\odot}$ close-to-solar metallicity models presented in Vescovi et al. (2020). Thus, we adopt for all the computed models their parameter choice for B_{φ} and u_p without further adjustments. We demand to a future work the analysis of the dependence of the magnetic mixing from the stellar core mass.

3. Results and discussion

In the following, we compare extant literature data and new FRUITY Magnetic models. In doing so, we adopt data from previous studies for intrinsic AGB carbon stars (Abia et al. 2010, 2011, 2015, 2019) and extrinsic CH/Ba stars (Lucatello et al. 2011). In Fig. 1 we report the [F/Fe] ratios of our selected sample as a function of the iron content [Fe/H]. We plot four group data: galactic (N-type) carbon stars, SC-type stars, extragalactic carbon stars, and extrinsic CH/Ba stars. Observational data are compared with stellar models of $1.5 M_{\odot}$ and $2 M_{\odot}$ at different TPs. Within the observational errors there is a good agreement, confirming the expected F-enhancement trend with the metallicity (see e.g. Lugaro et al. 2004; Cristallo et al. 2014). One word of caution has to be used regarding fluorine abundances in extrinsic CH/Ba stars, for which [F/Fe] ratios only represent lower limits due to dilution effects of binary mass-transfer phenomena (Abia et al. 2019).

The top panel of Fig. 2 shows the comparison between theoretical predictions of FRUITY Magnetic models with initial mass $M = 2 M_{\odot}$ and [Fe/H] ≥ -0.4 and spectroscopic observations for [F/Fe] ratios vs. the average s -element enhancement. Usually, four observational indices are used to represent s -process distributions and overabundances: [ls/Fe] (representative of the first s -process peak), [hs/Fe] (representative of the second s -process peak), [s/Fe], and [hs/ls]. Given the inhomogeneity of the available elemental abundance of heavy s -elements for the selected sample, we use the mean of the relative abundances of

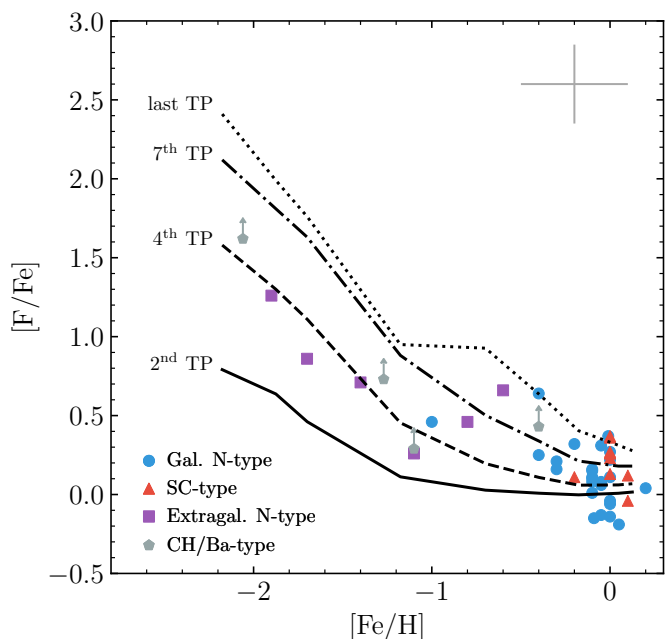


Fig. 1. Comparison between observed $[F/Fe]$ ratios as a function of the metallicity and FRUITY Magnetic models. Symbols refer to the four data groups: circles, galactic carbon stars; triangles, SC-type stars; squares, extragalactic carbon stars; pentagons, extrinsic CH/Ba stars. Lines represent theoretical predictions for 2 (for $[Fe/H] \geq -0.7$) and 1.5 M_{\odot} (for $[Fe/H] < -0.7$) AGB stars at different TPs. A typical error bar is indicated.

only Y and Zr to express the ls-index, and Ba and La to express the hs-index. The difference between the hs- and the ls-index quantifies the s-element index $[hs/ls]$, while the total average s-element enhancement is given by the mean of the relative abundances of Y, Zr, Ba, and La. For close-to-solar metallicity galactic N-type carbon stars (dots) and SC-type stars (triangles) the observed increase of fluorine with s-element enhancement is well reproduced by theoretical models. Note that the predicted $[F/Fe]$ are always positive since ^{19}F is overall produced in low-mass AGB stars (see also Lugaro et al. 2004). On the other hand, a few observational data show negative values which are, however, still consistent, within the errors, with no fluorine production. The comparison with N-type and extrinsic CH/Ba type stars (pentagon) with $[Fe/H] < -0.2$ is more challenging due to the smaller number of available information at these metallicities. In particular, two out of the three stars seems to exhibit the same trend observed at higher metallicity and are in good agreement with theoretical predictions, while the fluorine and s-elements abundances derived for TX Psc is slightly out of the trend and it is not fully reproduced by stellar models. This interpretation is confirmed even by considering $[F/s]$ ratios (see bottom panel of Fig. 2). Studying such an index, the fluorine enhancement for the extrinsic stars is not affected by uncertainties related to the dilution factor and provides a more robust tool for comparison. Confirming the previous analysis, models are able to replicate the quasi-linear decreasing trend of $[F/s]$ with the surface s-process enrichment, aside from the marginally-outside TX Psc. Given the typical uncertainties affecting observational data, however, it is difficult to firmly conclude that model predictions and observations are in disagreement for this single star.

Note that, in our computations we used the $^{13}C(\alpha, n)^{16}O$ reaction rate provided by Trippella & La Cognata (2017), which combined the latest asymptotic normalization coefficient values

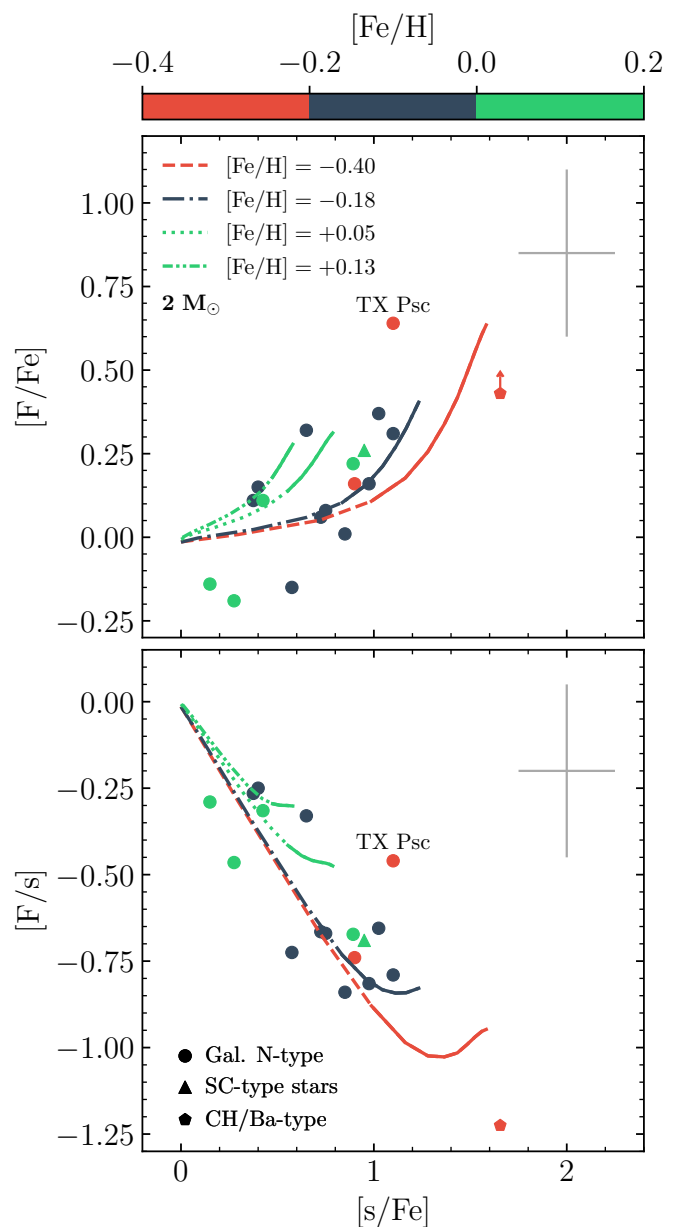


Fig. 2. Observed $[F/Fe]$ (top panel) and $[F/s]$ (bottom panel) vs. average s-element enhancements compared with theoretical predictions for 2 M_{\odot} and close-to-solar metallicity models. Symbols as in Fig. 1. Data points and theoretical lines are color-coded by $[Fe/H]$. The continuous portion of the lines represents the theoretical C-rich phase, while the discontinuous portion represents the O-rich phase. Typical uncertainties are shown. See text for details.

and the Trojan horse method, to determine the astrophysical S -factor with an indirect approach. At the typical temperature of ~ 90 MK corresponding to the radiative ^{13}C burning phase, the most recent direct measurement, given by Heil et al. (2008), is almost 20% higher. Adopting such a rate has however no impact in the production of s-nuclei if the ^{13}C pocket is fully consumed during the interpulse period (see also Trippella & La Cognata 2017). Instead, if some amount of ^{13}C survives, due to the lower reaction rate, it will be swallowed by the convective shell generated by the following TP and burnt at a rather high temperature (~ 200 MK), so providing an additional neutron burst and possibly affecting the production of s-nuclei and ^{19}F . This burst was shown to occur only during the very first TPs in low-mass

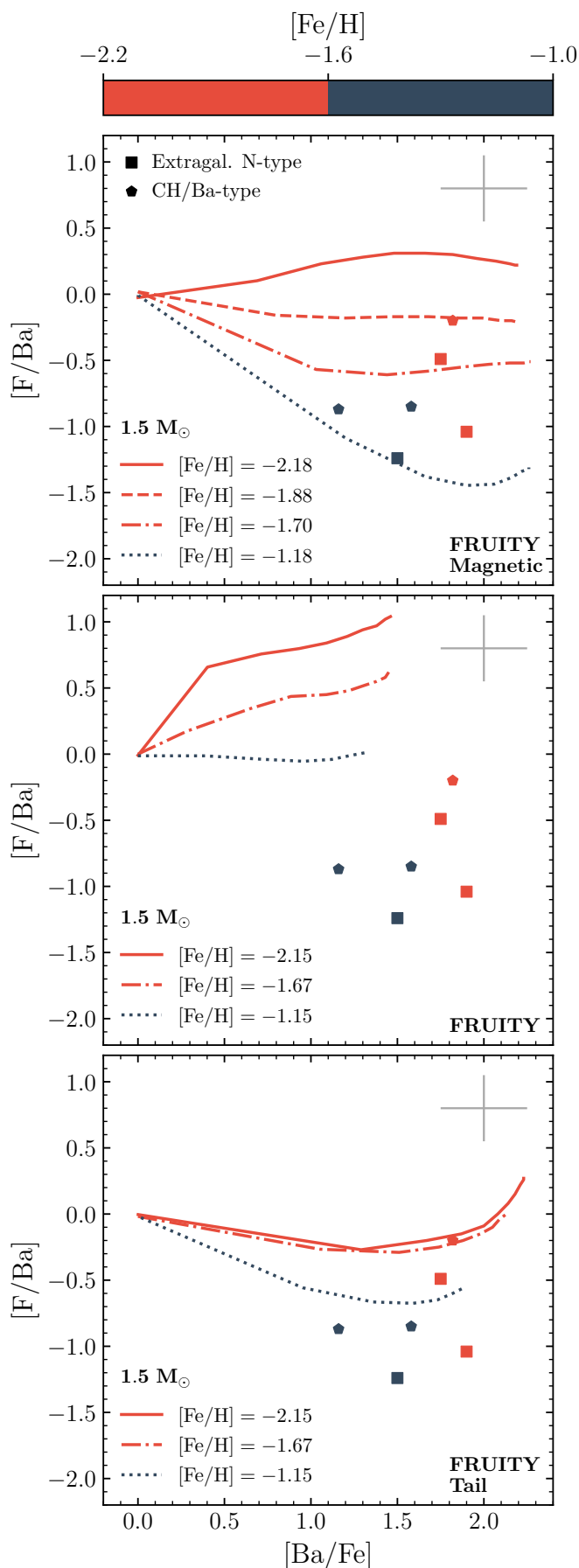


Fig. 3. $[F/Ba]$ vs. $[Ba/Fe]$ in the sample stars with $[Fe/H] \leq -1.0$. Symbols: squares, extragalactic carbon stars; pentagons, extrinsic CH/Ba stars. Lines are theoretical predictions for $1.5 M_{\odot}$ TP-AGB stars with low metallicity, assuming different mechanisms for the formation of the ^{13}C pocket (see text for details). Note that at these low metallicities, theoretical AGB models predict that the star becomes C-rich from first TDU episodes. Data points and theoretical lines are color-coded by $[Fe/H]$. Typical error bars are indicated.

AGB stars with high metallicity ($Z \geq 0.01$; see Cristallo et al. 2009b; Karakas 2010). In our $2 M_{\odot}$ $Z = 0.02$ model, switching from Trippella & La Cognata (2017) to Heil et al. (2008) reaction rate produces variations of less than 3% in $[F/Fe]$, $[ls/Fe]$, and $[hs/Fe]$ indexes, thus much lower than the typical uncertainties affecting spectroscopic observations of s-process-rich stars. Stellar models of lower metallicity are expected to produce even minor variations (Cristallo et al. 2009b; Karakas 2010) unless they have mass and metallicity so low ($M \lesssim 1.3 M_{\odot}$ and $[Fe/H] \lesssim -2.5$) to experience a proton ingestion episode at the first fully developed TP (see Cristallo et al. 2009a; Campbell et al. 2010; Choplin et al. 2021).

In Figures 3 and 4 we perform a similar comparison at low metallicities. Given the fact that there is no homogeneous sample of stars with both Ba and La, we compared model predictions separately. For both figures, we present in different panels theoretical expectations from new FRUITY Magnetic models (top panels), from standard FRUITY models (middle panels) and from FRUITY Tail models (bottom panels). Magnetic models are capable of well reproducing the spread observed, at different metallicities, for both $[F/Ba]$ and $[F/La]$ ratios as a function of the corresponding overall s-process enhancement. Conversely, standard FRUITY models fail in reproducing both the Ba and La enrichment, as well as the $[F/Ba]$ and $[F/La]$ ratios. Finally, FRUITY Tail models are sufficiently enriched in s-elements, due to the larger ^{13}C pockets than those obtained in standard FRUITY models, but still show a systematic over-production of fluorine with respect to Ba and La. As a whole, FRUITY Magnetic models show a reduction of fluorine production in good agreement to spectroscopic observations for low metallicity stars.

As previously mentioned, ^{19}F is primarily synthesized in AGB stars via the $^{15}\text{N}(\alpha, \gamma)^{19}\text{F}$ reaction reaction in the convective zone generated by a TP. The production of ^{15}N in the He-intershell involves a complex nuclear chain of successive n- (or p-) and α -captures starting from ^{13}C nuclei. A first source of ^{13}C is represented by the ^{13}C pocket itself, whose radiative burning leads to the accumulation of ^{15}N . A second source is the ^{13}C left in the H-burning shell ashes, which is engulfed into the convective zone generated by the TP and rapidly burned via the $^{13}\text{C}(\alpha, n)^{16}\text{O}$ reaction. In standard FRUITY models, the two channels almost equally contribute to the fluorine nucleosynthesis, especially at close-to-solar metallicity. On the other hand, moving to low metallicities the contribution of ^{13}C left in the H-burning ashes is less important (Cristallo et al. 2009b). Instead, in FRUITY Tail models, the larger ^{13}C pockets guarantee a net increase of s-process abundances and a large fluorine decrease at fixed s-process surface enhancement (Abia et al. 2015). However, these models barely reach negative values for $[F/Ba]$ and $[F/La]$ (see lower panels of Figures 3 and 4), pointing out that fluorine production need to be further suppressed, without altering the s-process enrichment (see also Abia et al. 2019). The extended profile and the low proton abundance characterizing FRUITY Magnetic models (Vescovi et al. 2020) have the twofold effect of forming large ^{13}C pockets and reducing the formation of primary ^{14}N . In this framework, the few available protons make first ^{13}C through the $^{12}\text{C}(p, \gamma)^{13}\text{C}$ reaction, preventing more proton captures to form ^{14}N and thereby inhibiting the nuclear chain $^{14}\text{N}(n, p)^{14}\text{C}(\alpha, \gamma)^{18}\text{O}(p, \alpha)^{15}\text{N}(\alpha, \gamma)^{19}\text{F}$. Hence, any fluorine appearing in AGB envelopes in these models is of secondary nature, generated by ^{14}N concentrations left behind by H-shell burning. This results in low fluorine enhancements and high s-enhancements, that pose FRUITY Magnetic models in close agreement with observations in very metal-poor AGB stars.

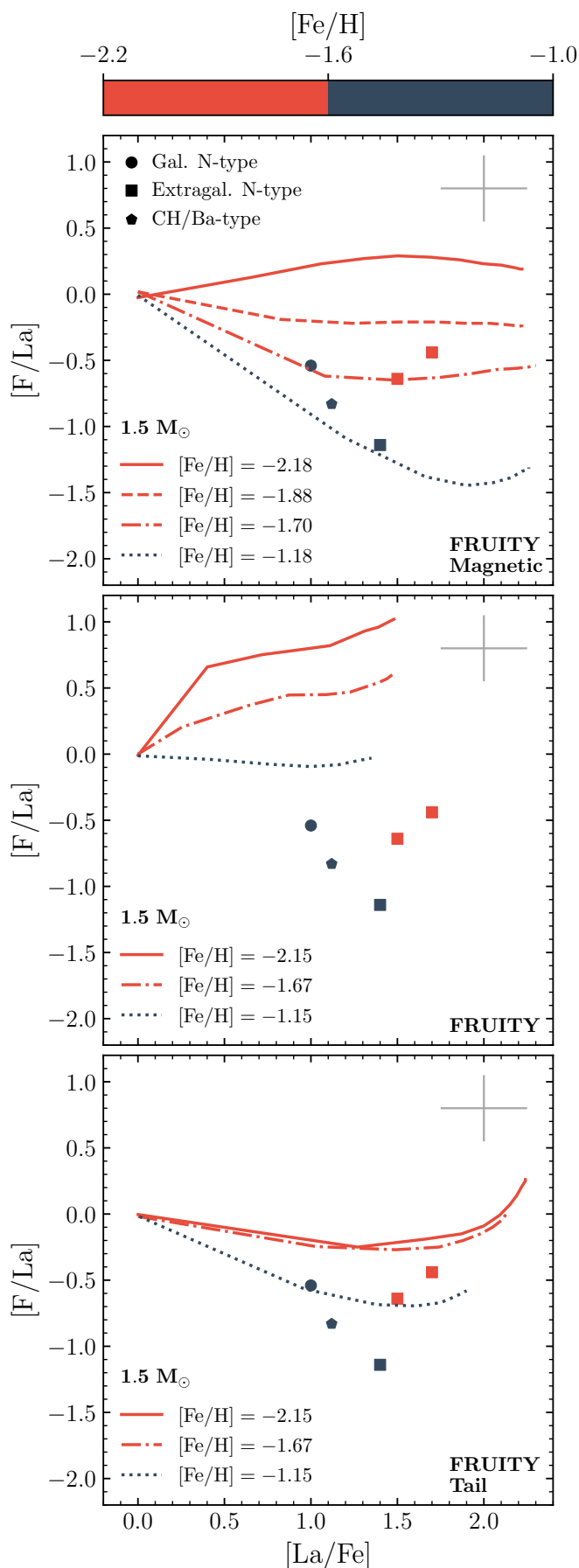


Fig. 4. Same as Fig. 3, but for $[F/La]$ vs. $[La/Fe]$.

4. Conclusions

The fluorine production in low-mass AGB stars has been revisited in the light of upgraded FRUITY stellar models, in which the ^{13}C neutron source is related to magnetic-buoyancy-induced phenomena. Predicted fluorine enhancements are in agreement with those observed in carbon stars at different metallicities. The observed correlation between F and the s-element enhancements is also reproduced. On one hand, new FRUITY Magnetic models show a reduced net ^{19}F production, with respect to models in which the partial mixing of hydrogen during a TDU is attributed to overshooting below the convective envelope of an AGB star. This is a consequence of the low abundance of ^{14}N in the ^{13}C pocket, which leads to a negligible production of fluorine during the ^{13}C radiative burning. The ^{19}F envelope abundance is therefore ascribed only to the amount of the secondary ^{13}C in the H-shell ashes, which depends on the CNO abundances in the star. On the other hand, mixing induced by magnetic buoyancy leads to extended ^{13}C pockets so resulting in large surface s-process enrichments. As a whole, new FRUITY Magnetic models simultaneously accounts for both the observed fluorine and the average s-element enhancements in intrinsic AGB carbon stars and extrinsic CH/Ba stars.

Different types of data (presolar grain measurements and spectroscopic observations) related to stars belonging to different components of our Galaxy (disk and halo) point to a single configuration of mixing induced by magnetic buoyancy.

The above scenario suggests that magnetism should also be a quite common phenomenon in evolved low-mass stars. In this respect, there exists several observations of magnetic fields of a few G in the envelopes of AGB stars (see, e.g., Vlemmings 2019 and references therein). Another piece of evidence for magnetic fields in low-mass stars is provided by the increasing number of observed magnetic white dwarfs (WDs). During the least decades, many of WDs lying within 20 pc from the Sun revealed to have field strength above ~ 1 MG, while for most of them the available data were not sufficient to assess the presence or not of magnetic fields. These studies suggested that about 10% of all white dwarfs are magnetic (e.g. Kawka et al. 2007). However, the advent of increasingly precise spectroscopic and spectropolarimetric observations, which improve the capability to detect magnetic fields of low strength, revealed that at least $\sim 20\%$ of WDs possess magnetic fields ranging from a few kG up to about 1000 MG (Landstreet & Bagnulo 2019; Bagnulo & Landstreet 2020), indicating that magnetism is a widespread, rather than a rare, property of WDs. These magnetic fields are most likely leftovers of previous phases, and they may be the result of a complicated interaction between fossil and dynamo generated fields during stellar evolution and/or stellar merger events (Ferrario et al. 2020). In our scenario, we propose that, below the extended convective envelope of low-mass AGB stars, strong toroidal magnetic fields exist and trigger a magnetic-buoyant-induced mixing adequate for the formation of the ^{13}C pocket. The required mixing rate put constraints on the field strength. In this picture, the toroidal field is assumed to originate from a dynamo operating in the AGB interiors which amplifies a small seed poloidal field by draining the available differential rotation energy.

The present study provides another, independent, confirmation (see Magrini et al. 2021) that the calibration performed by Vescovi et al. (2020) on the free parameters characterizing magnetic buoyancy-induced mixing is extremely robust. However, additional analyses are needed to validate such a statement, before claiming for a definitive theory.

Acknowledgements. DV and SC acknowledge S. Bagnulo for fruitful discussions. DV acknowledges financial support from the German-Israeli Foundation (GIF No. I-1500-303.7/2019). CA acknowledges financial support from the Agencia Estatal de Investigación of the Spanish Ministerio de Ciencia e Innovación through the FEDER funds projects PGC2018-095317-B-C2.

References

- Abia, C., Cristallo, S., Cunha, K., de Laverny, P., & Smith, V. V. 2019, *A&A*, 625, A40
- Abia, C., Cunha, K., Cristallo, S., & de Laverny, P. 2015, *A&A*, 581, A88
- Abia, C., Cunha, K., Cristallo, S., et al. 2010, *ApJ*, 715, L94
- Abia, C., Cunha, K., Cristallo, S., et al. 2011, *ApJ*, 737, L8
- Abia, C., de Laverny, P., Cristallo, S., Kordopatis, G., & Straniero, O. 2020, *A&A*, 633, A135
- Abia, C., Recio-Blanco, A., de Laverny, P., et al. 2009, *ApJ*, 694, 971
- Angulo, C., Arnould, M., Rayet, M., et al. 1999, *Nucl. Phys. A*, 656, 3
- Bagnulo, S. & Landstreet, J. D. 2020, *A&A*, 643, A134
- Battino, U., Lederer-Woods, C., Cseh, B., Denissenkov, P., & Herwig, F. 2021, *Universe*, 7, 25
- Battino, U., Pignatari, M., Ritter, C., et al. 2016, *ApJ*, 827, 30
- Best, A., Pantaleo, F. R., Boeltzig, A., et al. 2019, *Physics Letters B*, 797, 134900
- Bruno, C. G., Aliotta, M., Descouvemont, P., et al. 2019, *Physics Letters B*, 790, 237
- Bruno, C. G., Scott, D. A., Aliotta, M., et al. 2016, *Phys. Rev. Lett.*, 117, 142502
- Busso, M., Gallino, R., & Wasserburg, G. J. 1999, *ARA&A*, 37, 239
- Busso, M., Vescovi, D., Palmerini, S., Cristallo, S., & Antonuccio-Delogu, V. 2021, *ApJ*, 908, 55
- Busso, M., Wasserburg, G. J., Nollett, K. M., & Calandra, A. 2007, *ApJ*, 671, 802
- Campbell, S. W., Lugaro, M., & Karakas, A. I. 2010, *A&A*, 522, L6
- Choplin, A., Siess, L., & Goriely, S. 2021, *A&A*, 648, A119
- Cristallo, S., Abia, C., Straniero, O., & Piersanti, L. 2015a, *ApJ*, 801, 53
- Cristallo, S., Di Leva, A., Imbriani, G., et al. 2014, *A&A*, 570, A46
- Cristallo, S., La Cognata, M., Massimi, C., et al. 2018, *ApJ*, 859, 105
- Cristallo, S., Piersanti, L., Straniero, O., et al. 2011, *ApJS*, 197, 17
- Cristallo, S., Piersanti, L., Straniero, O., et al. 2009a, *PASA*, 26, 139
- Cristallo, S., Straniero, O., Gallino, R., et al. 2009b, *ApJ*, 696, 797
- Cristallo, S., Straniero, O., Lederer, M. T., & Aringer, B. 2007, *ApJ*, 667, 489
- Cristallo, S., Straniero, O., Piersanti, L., & Gobrecht, D. 2015b, *ApJS*, 219, 40
- D'Agata, G., Pizzone, R. G., La Cognata, M., et al. 2018, *ApJ*, 860, 61
- Denissenkov, P. A. & Tout, C. A. 2003, *MNRAS*, 340, 722
- Di Leva, A., Scott, D. A., Caciolli, A., et al. 2014, *Phys. Rev. C*, 89, 015803
- Ferrario, L., Wickramasinghe, D., & Kawka, A. 2020, *Advances in Space Research*, 66, 1025, nova Eruptions, Cataclysmic Variables and Related Systems: Challenges in the 2020 Era
- Forestini, M., Goriely, S., Jorissen, A., & Arnould, M. 1992, *A&A*, 261, 157
- Goriely, S. & Mowlavi, N. 2000, *A&A*, 362, 599
- Grisoni, V., Romano, D., Spitoni, E., et al. 2020, *MNRAS*, 498, 1252
- Guandalini, R. & Cristallo, S. 2013, *A&A*, 555, A120
- Heil, M., Detwiler, R., Azuma, R. E., et al. 2008, *Phys. Rev. C*, 78, 025803
- Herwig, F. 2005, *ARA&A*, 43, 435
- Herwig, F., Bloeker, T., Schoenberner, D., & El Eid, M. 1997, *A&A*, 324, L81
- Herwig, F., Langer, N., & Lugaro, M. 2003, *ApJ*, 593, 1056
- Iben, I., J. & Renzini, A. 1983, *ARA&A*, 21, 271
- Iliadis, C., Longland, R., Champagne, A. E., Coc, A., & Fitzgerald, R. 2010, *Nuclear Physics A*, 841, 31
- Imbriani, G., Costantini, H., Formicola, A., et al. 2005, *European Physical Journal A*, 25, 455
- Indelicato, I., La Cognata, M., Spitaleri, C., et al. 2017, *ApJ*, 845, 19
- Johnson, E. D., Rogachev, G. V., Mitchell, J., Miller, L., & Kemper, K. W. 2009, *Phys. Rev. C*, 80, 045805
- Jorissen, A., Smith, V. V., & Lambert, D. L. 1992, *A&A*, 261, 164
- José, J. & Hernanz, M. 1998, *ApJ*, 494, 680
- Joyce, M. & Chaboyer, B. 2018, *ApJ*, 856, 10
- Karakas, A. I. 2010, *MNRAS*, 403, 1413
- Karakas, A. I. & Lattanzio, J. C. 2014, *PASA*, 31, e030
- Kawka, A., Vennes, S., Schmidt, G. D., Wickramasinghe, D. T., & Koch, R. 2007, *ApJ*, 654, 499
- Kobayashi, C., Izutani, N., Karakas, A. I., et al. 2011, *ApJ*, 739, L57
- Landstreet, J. D. & Bagnulo, S. 2019, *A&A*, 628, A1
- Leblanc, P. J., Imbriani, G., Görres, J., et al. 2010, *Phys. Rev. C*, 82, 055804
- Limongi, M. & Chieffi, A. 2018, *ApJS*, 237, 13
- Lodders, K. 2020, *Solar Elemental Abundances*
- Lucatello, S., Masseron, T., Johnson, J. A., Pignatari, M., & Herwig, F. 2011, *ApJ*, 729, 40
- Lugaro, M., Ugalde, C., Karakas, A. I., et al. 2004, *ApJ*, 615, 934
- Magrini, L., Vescovi, D., Casali, G., et al. 2021, *A&A*, 646, L2
- Marigo, P. 2002, *A&A*, 387, 507
- Marigo, P. & Aringer, B. 2009, *A&A*, 508, 1539
- Meynet, G. & Arnould, M. 2000, *A&A*, 355, 176
- Nucci, M. C. & Busso, M. 2014, *ApJ*, 787, 141
- Olive, K. A. & Vangioni, E. 2019, *MNRAS*, 490, 4307
- Palmerini, S., Trippella, O., Busso, M., et al. 2018, *Geochim. Cosmochim. Acta*, 221, 21
- Piersanti, L., Cristallo, S., & Straniero, O. 2013, *ApJ*, 774, 98
- Prantzos, N., Abia, C., Limongi, M., Chieffi, A., & Cristallo, S. 2018, *MNRAS*, 476, 3432
- Renda, A., Fenner, Y., Gibson, B. K., et al. 2004, *MNRAS*, 354, 575
- Siess, L., Goriely, S., & Langer, N. 2004, *A&A*, 415, 1089
- Spitoni, E., Matteucci, F., Jönsson, H., Ryde, N., & Romano, D. 2018, *A&A*, 612, A16
- Straniero, O., Gallino, R., & Cristallo, S. 2006, *Nuclear Physics A*, 777, 311
- Trippella, O., Busso, M., Maiorca, E., Käppeler, F., & Palmerini, S. 2014, *ApJ*, 787, 41
- Trippella, O., Busso, M., Palmerini, S., Maiorca, E., & Nucci, M. C. 2016, *ApJ*, 818, 125
- Trippella, O. & La Cognata, M. 2017, *ApJ*, 837, 41
- Ventura, P. & Marigo, P. 2010, *MNRAS*, 408, 2476
- Vescovi, D., Cristallo, S., Busso, M., & Liu, N. 2020, *ApJ*, 897, L25
- Vescovi, D., Piersanti, L., Cristallo, S., et al. 2019, *A&A*, 623, A126
- Vlemmings, W. 2019, *IAU Symposium*, 343, 19
- Wallner, A., Bichler, M., Buczak, K., et al. 2016, *Phys. Rev. C*, 93, 045803
- Woodsley, S. E. & Haxton, W. C. 1988, *Nature*, 334, 45